


Article

Advancing Borehole Imaging: A Classification Database Developed via Adaptive Ring Segmentation

Zhaopeng Deng ¹, Shuangyang Han ¹, Zeqi Liu ¹, Jian Wang ²  and Haoran Zhao ^{1,*}¹ School of Information and Control Engineering, Qingdao University of Technology, Qingdao 266520, China² College of Science, China University of Petroleum (East China), Qingdao 266580, China

* Correspondence: zhaohaoran@qut.edu.cn

Abstract: The use of in-hole imaging to investigate geological structure characteristics is one of the crucial methods for the study of rock mass stability and rock engineering design. The in-hole images are usually influenced by the lighting and imaging characteristics, resulting in the presence of interference noise regions in the images and consequently impacting the classification accuracy. To enhance the analytical efficacy of in-hole images, this paper employs the proposed optimal non-concentric ring segmentation method to establish a new database. This method establishes the transformation function based on the Ansel Adams Zone System and the fluctuation values of the grayscale mean, adjusting the gray-level distribution of images to extract two visual blind spots of different scales. Thus, the inner and outer circles are located with these blind spots to achieve the adaptive acquisition of the optimal ring. Finally, we use the optimal non-concentric ring segmentation method to traverse all original images to obtain the borehole image classification database. To validate the effectiveness of this method, we conduct experiments using various segmentation and classification evaluation metrics. The results show that the Jaccard and Dice of the optimal non-concentric ring segmentation approach are 88.43% and 98.55%, respectively, indicating superior segmentation performance compared to other methods. Furthermore, after employing four commonly used classification models to validate the performance of the new classification database, the results demonstrate a significant improvement in accuracy and macro-average compared to the original database, with the highest increase in accuracy reaching 4.2%. These results fully demonstrate the effectiveness of the proposed optimal non-concentric ring segmentation method.



Citation: Deng, Z.; Han, S.; Liu, Z.; Wang, J.; Zhao, H. Advancing Borehole Imaging: A Classification Database Developed via Adaptive Ring Segmentation. *Electronics* **2024**, *13*, 1107. <https://doi.org/10.3390/electronics13061107>

Academic Editor: Luca Mesin

Received: 3 January 2024

Revised: 6 March 2024

Accepted: 12 March 2024

Published: 18 March 2024



Copyright: © 2024 by the authors. Licensee MDPI, Basel, Switzerland. This article is an open access article distributed under the terms and conditions of the Creative Commons Attribution (CC BY) license (<https://creativecommons.org/licenses/by/4.0/>).

Keywords: intelligent analysis and processing; computer vision; image classification; image segmentation; data optimization

1. Introduction

With the increasing demand for resources, projects in various fields, such as tunnel excavation, oil exploration, and mining, are on the rise. In these projects, geological exploration becomes crucial, especially in the study of rock structure surfaces [1]. A rock mass consists of rock blocks separated by structural surfaces, and the characteristics of these surfaces directly impact the stability, mechanical properties, and engineering features of the rock mass. Due to different tectonic movements in different geological periods, various types of structural surfaces form in the rock mass, including fissures, faults, joints, detachments, fracture zones, weak zones, and weak layers. These structural surfaces constitute the most vulnerable parts of the rock mass, determining the engineering geological characteristics and overall stability of the rock mass. Therefore, the in-depth analysis and study of rock structure surfaces have become an essential task in geological exploration.

To gain a deeper understanding of the internal structure of rock formations, it is necessary to employ specialized techniques and equipment to observe their internal features. With the continuous advancement of borehole camera technology, this technology has found widespread application in various fields, such as engineering geological exploration,

rock mass integrity assessment, mining engineering, and petroleum development. Devices based on optical technology can capture 360° borehole wall videos or images, recording crucial information about the distribution, development characteristics, and geometric parameters of internal rock structures. This information is essential for geological exploration and the design of rock and soil engineering projects. However, the processing and analysis of borehole image data require significant time and manpower, and human factors may introduce subjective results. Therefore, to enhance the efficiency and accuracy of processing and analysis, particularly for large geological datasets, efficient automation methods are indispensable.

Drilling imaging technology often captures geological borehole images that exhibit interference regions, including quasi-circular shadow areas and edge distortions. These are attributed to the effects of lighting and camera principles within the borehole. Interference factors, such as quasi-circular shadow regions and edge distortion, significantly impact the accuracy and reliability of applications like feature extraction [2,3], image recognition, and geological structure analysis. The analysis of geological borehole images requires the use of appropriate algorithms and techniques, including image denoising [4], enhancement [5], segmentation [6], etc., to improve the image recognition accuracy and information acquisition efficiency. Thus, constructing a geological borehole image recognition database through image segmentation technology [7,8] can significantly enhance the efficiency in processing [9–11] and analyzing geological borehole images, reducing the manual processing burden and minimizing the potential for errors.

When analyzing the experimental results of the literature related to image segmentation, it was observed that the application domains of existing image segmentation methods do not align with geological borehole images. The extracted features from these methods differ significantly from the characteristics of geological borehole images. Therefore, when applying these methods to geological borehole images, it is often challenging to achieve the desired segmentation results. To enhance the segmentation quality and obtain a more optimal dataset, this paper proposes an optimal non-concentric ring segmentation method to establish a new database. The experimental results indicate that, compared to the original images, the new database not only eliminates noise interference regions in the images but also achieves higher classification accuracy. In summary, the contributions of this work encompass the following aspects.

- By employing the optimal non-concentric ring segmentation method proposed in this paper, we are able to remove interference regions within the images and extract the region of interest (ROI). This process helps to reduce the proportion of irrelevant information in the image feature data, thereby extracting geological features that are more representative and critical.
- Dynamic grayscale transformation intervals are constructed to optimize the image segmentation results.
- Constructing the geological borehole image classification database involves implementing the proposed optimal non-concentric ring segmentation method and comparing it with the original database using various classification models.

The structure of the remaining sections of this paper is as follows. The related work is reviewed in Section 2. Section 3 provides a comprehensive explanation of the proposed optimal non-concentric ring segmentation method and outlines the process of constructing the geological borehole image classification database. In Section 4, we discuss the experimental results. Finally, Section 5 serves as the conclusion for this presentation.

2. Related Works

For image datasets obtained from borehole camera systems, various processing methods are commonly employed to improve the data processing efficiency and enhance the visual effects. These methods encompass image enhancement, feature extraction, multi-dimensional modeling, image classification, and image segmentation, among others. Zou et al. [12] proposed a high-resolution borehole image rapid synthesis method,

capable of enhancing both the horizontal and vertical resolutions of the images to 0.1 mm, enabling the finer detection of rock structure features. Guo and Wang [13] proposed a multiple-point geostatistical method, introducing a mobile local scanning approach. This method enables simulation nodes to scan within specific zoom areas, achieving partition simulation effects concurrently and addressing discontinuity issues between partition boundaries. The approach is instrumental in directly reconstructing a three-dimensional geological model from borehole data. It proves effective in revealing the morphology of stratigraphic structures, layer properties, and relationships between different geological layers. Mirkes et al. [14] demonstrated a pseudo-outcrop visualization method for borehole and full-diameter rock core images, aiming to augment the ubiquitous unwrapped cylinder view and assist non-specialist interpreters. The pseudo-outcrop visualization is equivalent to a nonlinear projection of the image from the borehole to an earth frame of reference, creating a solid volume sliced longitudinally to reveal two or more faces.

In the field of geological image classification, Ma et al. [15] designed a learning architecture based on knowledge distillation and a high-accuracy feature localization comparison network (FPCN) for the generation of small yet high-performance rock image classification models. The architecture involves the interaction of feature vectors generated from local feature maps of two images, capturing both common and distinctive features. This enables the network to focus on more complementary information across different scales for various objects. Subsequently, the model learns the essential features of the images in this manner, providing crucial discriminative information for the micro-model through model distillation. Zhou and colleagues [16] proposed and implemented a next-generation convolutional neural network (CNN) named HKUDES_Net, designed to classify seven rock types with similar textures and colors. Leveraging computational strategies such as dynamic dilation and squeeze-and-excitation, HKUDES_Net can effectively classify rock types with varying granularity.

In the field of image segmentation, the classic methods include threshold-based [17], clustering-based [18], and edge-based approaches. Matica et al. [19] proposed a real-time Biscuit Tile Segmentation (BTS) method, which is based on signal change detection and contour tracing. This method aims to separate tile pixels from the background in images captured on the production line. A fault-tolerant quantum dual-threshold algorithm has been proposed by Lopez et al. [20], constructed using Clifford+T gates and compatible with error detection and correction codes. This integration enhances the noise tolerance, reduces the computational costs, and adds fault tolerance to the existing dual-threshold segmentation approach. Bayá [21] employed a clustering validation method, clustering stability (CS), for automatic image segmentation. CS is not constrained by the dimensions of the image or the clustering algorithm and is capable of determining the optimal number of partitions based on color and texture features.

In recent years, with the continuous development of deep learning networks, their applications have been expanding. Deep learning methods [22], such as convolutional neural networks (CNNs), have been successfully applied to image segmentation tasks in various domains [23,24], including natural images, satellite images, and medical images, achieving remarkable results. Islam et al. [25] proposed a lightweight convolutional network, LUVS-Net. The network utilizes an encoder–decoder framework, wherein edge data are transposed from the first layer of the encoder to the last layer of the decoder, significantly improving the convergence speed. Fan et al. [26] proposed a method that integrates a hierarchical strategy into an image matting model for blood vessel segmentation in fundus images. This approach utilizes the features of vascular regions to generate a ternary map, and then applies a hierarchical image matting model to extract vessel pixels from unknown regions. However, these methods are primarily tailored to their respective domain images. Due to the specific nature of the capture perspective and environment in borehole camera systems, the features of geological borehole images are notably different from those of other images. Therefore, other image segmentation methods cannot be directly applied to geological borehole images. In this paper, considering the characteristics of geological

borehole images, we propose an optimal non-concentric ring segmentation method to establish a new database.

3. Materials and Methods

3.1. Analysis of Original Image Data

The original geological borehole images used in this study are 360-degree hole wall images obtained by moving the forward-looking borehole camera system radially in a pre-drilled slender cylindrical hole. The system can map the three-dimensional hole wall images within the effective illumination region in front of the probe into the two-dimensional plane images, similar to observing the three-dimensional space of a cylinder through a circular window. The geological borehole images are mainly divided into three categories, namely border images, intact rock images, and fracture images.

The border images mainly include coal rock boundary images and the boundary images of different rock masses. These images exhibit significant variations in texture features, typically characterized by rough and irregular textures. At the interface, the grayscale variation of the image is significant, as shown in Figure 1a. The intact rock images are relatively complete borehole wall images, with a smooth and delicate surface, a single color feature, and small changes in texture and grayscale features, as shown in Figure 1b. The fracture images are hole wall images that include destructive structures such as abscission layers, fractures, joints, rupture regions, and so on, as shown in Figure 1c.

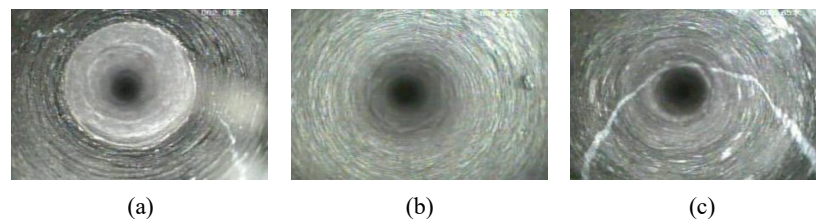


Figure 1. Three types of geological borehole images. (a) Border image. (b) Intact rock image. (c) Fracture image.

The forward-viewing borehole camera technology captures images of the borehole wall in front of the probe using a CCD camera installed at the top of the probe. Due to the borehole channel being a slender cylindrical space with an uneven medium on its inner surface, the light emitted by the probe's illumination device scatters continuously during the reflection process. This scattering results in the appearance of a quasi-circular shadow region (QSR) at the center of the image, as shown in the Figure 2. In addition, according to the principle of in-hole imaging, in the process of mapping a cylindrical three-dimensional space image into a two-dimensional plane image, the generated two-dimensional image will produce varying degrees of geometric distortion as the angle increases when the viewing angle of the wide-angle lens is greater than 90° . Therefore, there is an obvious edge distortion region (EDR) in the edge imaging region of geological borehole images, as illustrated in Figure 2.

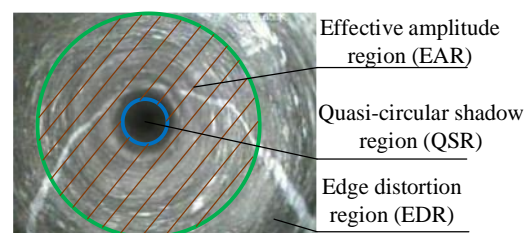


Figure 2. Distribution map of borehole image regions.

In general, the QSRs in different types of borehole images share similar image characteristics, such as position, shape, texture, and color, making them challenging for image type discrimination. This region occupies a significant portion of the entire image but does not contribute meaningful features for image recognition. Therefore, the significance of this region is relatively low, diluting the weight of valuable information in image feature representation. It has no positive effect on the image recognition process, but rather serves as an interference region.

In addition, the two-dimensional plane image of cylindrical spatial mapping can be viewed as being composed of continuous annular regions, where the degree of distortion in these annular regions gradually increases outward from the two-dimensional axis of the cylindrical drill, and the drilling center is usually not located at the geometric center of the image. In this paper, the EDR is situated at the boundaries of the rectangular image, which is an incomplete ring with severe geometric distortion. Therefore, the EDR can also be regarded as an interference region with a limited positive impact on the recognition process.

3.2. Overview of Dynamic Construction Method of Geological Borehole Image Recognition Database

When performing image recognition or big data analysis on the original borehole image database, the presence of the QSR and the EDR might generate a large number of image noise regions, which can impact the image analysis results. To solve this problem, this study proposes a dynamic construction method for a borehole image recognition database based on the optimal non-concentric ring segmentation algorithm (ONRS). Taking the original geological borehole images as the research object, the proposed ONRS algorithm is used to extract the region of interest (ROI) from the original images, and then it is cyclically processed with the original image data to build a geological borehole image recognition database. The database construction process is shown in Figure 3, which is mainly divided into three steps, namely extracting adaptive dual-scale visual blind spots, segmenting the optimal non-concentric ring region, and building the geological borehole image recognition database.

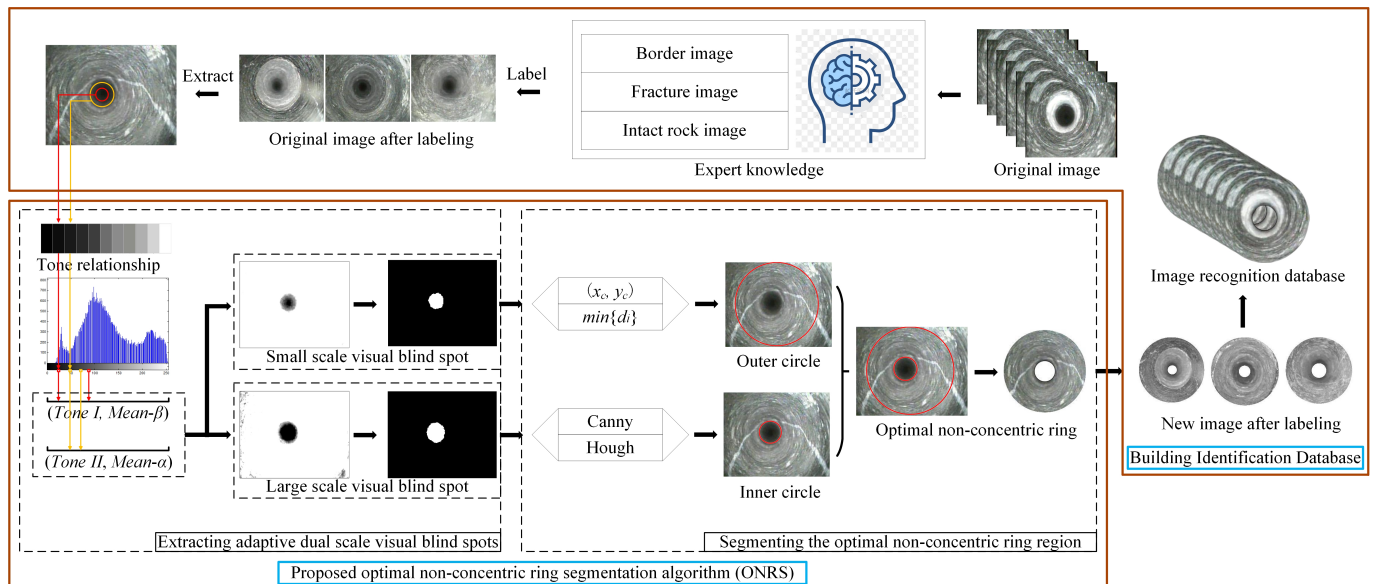


Figure 3. Dynamic construction flowchart of geological borehole image recognition database.

(1) Extracting adaptive dual-scale visual blind spots.

According to the tone relationship of the Ansel Adams Zone System, the first and second tones (*Tone I* and *Tone II*) are used for grayscale mapping to obtain the corresponding two grayscale values. These grayscale values serve as the minimum values of the transformation interval, and the two fluctuation values of the average grayscale value (*Mean- α* and

$Mean-\beta$) serve as the maximum values, which form the grayscale transformation intervals (($Tone I-Mean-\alpha$) and ($Tone II-Mean-\beta$)). Then, using the segmented functions constructed from these intervals to optimize the grayscale distribution, two grayscale images with different scales are obtained. Subsequently, the Otsu algorithm is applied to the grayscale images to perform binarization. Post-binarization, clutter filtering is executed on the binary images to obtain the adaptive dual-scale visual blind spots, i.e., large-scale and small-scale visual blind spots.

(2) Segmenting the optimal non-concentric ring region.

We use the Hough transform to obtain the fitting circles of the large-scale visual blind spots and set threshold γ to expand the fitting circle radius to gain the optimal inner circle, thereby achieving full inclusion for the QSR. Simultaneously, the 2D axis coordinate of a drilling cylinder (centroid of the small-scale visual blind spot) is determined, and it is used as the center to select the minimum inscribed circle as the optimal outer circle to eliminate the EDR. Through these methods, we can achieve the segmentation of the optimal non-concentric ring region.

(3) Building the geological borehole image recognition database.

All original borehole images are labeled using expert knowledge, which are then traversed based on the proposed ONRS algorithm to obtain the optimal non-concentric ring borehole image with labels. Ultimately, the image set is organized and summarized to complete the dynamic construction of the geological borehole image recognition database.

3.3. Extracting Adaptive Dual-Scale Visual Blind Spots

The ONRS algorithm proposed in this paper adaptively acquires dual-scale visual blind spots (comprising both large-scale and small-scale visual blind spots) with the grayscale distribution of borehole images, aiming to eliminate the QSR and the EDR from the original images. Among them, the large-scale and small-scale visual blind spots are employed to extract the inner and outer circles of the optimal non-concentric ring regions, respectively. The extraction process is shown in Figure 4 and is primarily divided into two parts.

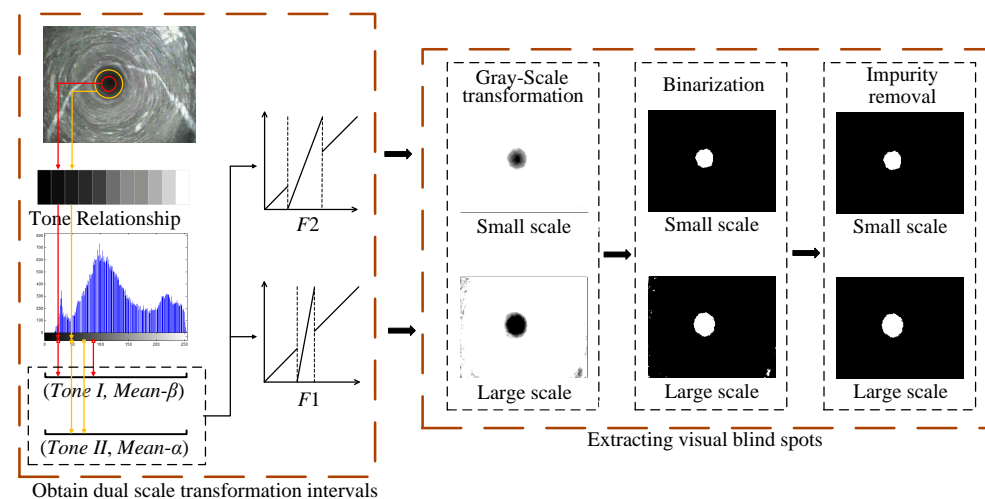


Figure 4. Flowchart of the adaptive dual-scale visual blind spot extraction method.

(1) Obtaining adaptive dual-scale gray-level transformation intervals.

In this part, based on the correspondence between image tones and grayscale values in the Ansel Adams Zone System, the grayscale mappings of the first tone ($Tone I$) and the second tone ($Tone II$) are extracted as the minimum values for the small-scale and large-scale grayscale transformation intervals, which correspond to the small-scale and large-scale visual blind spots, respectively. Simultaneously, we calculate the average grayscale values of the borehole images using grayscale histograms and experimentally determine the

fluctuation values [27,28] of these two average grayscale values to act as the maximum values, forming the dual-scale grayscale transformation interval.

(2) Extracting visual blind spots.

According to the grayscale transformation intervals ((*Tone I-Mean- α*) and (*Tone II-Mean- β*)), the segmented functions *F1* and *F2* are constructed to optimize the grayscale distribution of the borehole images, obtaining two grayscale images at different scales. Subsequently, the Otsu algorithm is employed for image binarization. After removing the clutter and black spots from the binary images, the acquisition of the adaptive dual-scale visual blind spots is thus achieved.

3.3.1. Obtaining the Dual-Scale Gray Transformation Intervals

Before obtaining the dual-scale visual blind spots, it is necessary to perform grayscale transformation on the original images. This transformation emphasizes the edge information of the visual blind spots and effectively distinguishes between visual blind spots and effective amplitude regions. This article adaptively obtains the dual-scale grayscale transformation interval that matches the original image based on the image tone under the 18% gray reflectance benchmark in the Ansel Adams Zone System and the fluctuation value of the average grayscale value.

The Ansel Adams Zone System [29] is one of the fundamental theories in photographic science. It divides the grayscale range of an image into 11 tonal zones, from the darkest zero zone (the blackest part that the photo can represent) to the tenth zone (the background color of the photo, which is white). During the photographic process, 18% gray is used as the benchmark for metering. Due to the logarithmic relationship between the brightness reflected and the surface grayscale of an object, 18% gray corresponds to 50% of the reflected light brightness. The corresponding relationship between the image tones and the grayscale values under the 18% gray reflectance benchmark is shown in Table 1.

Table 1. Mapping relationship between image tonal zones and gray levels.

% Black	100%	90%	80%	70%	60%	50%	40%	30%	20%	10%	0%
Tone	0	I	II	III	IV	V	VI	VII	VIII	IX	X
Grayscale	0	26	51	77	102	128	153	179	204	230	255
	Low tone regions			Mid tone regions			High tone regions				

According to the Ansel Adams Zone System, different tonal zones have different reflectivity, and its corresponding tone colors (grayscale values) are also different. Based on the 18% gray benchmark, the 0 to X tonal zones correspond to 11 grayscale colors from deep black to light white, respectively. Typically, these 11 grayscale values are divided into three groups: the first group (tonal zones 0 to III) corresponds to the low-tone regions, the second group (tonal zones IV to VI) corresponds to the mid-tone regions, and the third group (tonal zones VII to X) corresponds to the high-tone regions. Additionally, tonal zones II to VIII are often referred to as the texture amplitude, representing texture details and subtle variations in the image. Tonal zones I to IX are referred to as the effective amplitude, representing the detailed information and visual effects of the image. Tonal zones 0 to X are often referred to as the full tone, covering the entire grayscale range of the image, as shown in Figure 5. For the geological borehole images studied in this article, the QSR belongs to the region outside the effective amplitude, while the optimal non-concentric ring region and the EDR are both within the effective amplitude region.

For the minimum value of the grayscale transformation interval, this article uses the grayscale values corresponding to different tones. When selecting the grayscale value corresponding to the second tonal zone (*Tone II*) as the minimum value, the image segmentation effect is closest to the standard large-scale visual blind spot range. Additionally, as the size of the small-scale visual blind spot decreases, the error between the centroid

coordinates and the true two-dimensional axis center coordinates of the drilling cylinder will also decrease. After verification, the experimental effect is best when the grayscale value corresponding to the first tonal zone (*Tone I*) is taken as the minimum value in the small-scale transformation interval. Therefore, this paper selects *Tone II* and *Tone I* as the minimum values of the grayscale transformation intervals for large- and small-scale visual blind spots, respectively.

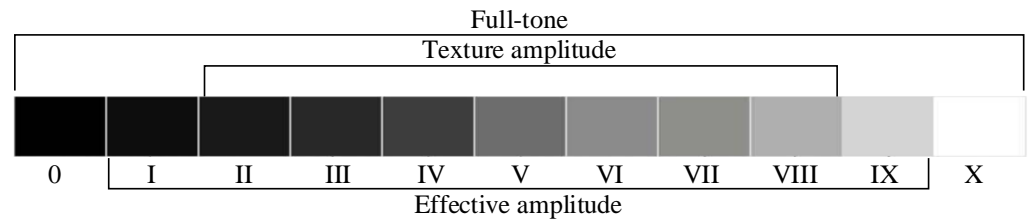


Figure 5. Tonal zones corresponding to different amplitudes.

For the maximum value of the grayscale transformation interval, due to the overall grayscale difference of each borehole image, the optimal segmentation of the QSR cannot be achieved when a fixed value is selected as the maximum value of the grayscale transformation interval. Therefore, aiming at the segmentation effect of the two visual blind spots, this paper determines the two fluctuation values as the maximum values of the gray transformation intervals, by optimizing the parameters based on the average gray value. This approach can not only ensure the integrity of the QSR in different types of borehole images, but also allows one to automatically adjust the optimal range of the region according to the gray distribution of each image.

Finally, this paper takes *Tone I* and *Tone II* as the minimum values and the fluctuation values of the average gray value as the maximum values to form the dual-scale gray transformation intervals ($(\textit{Tone I} - \textit{Mean} - \alpha)$ and $(\textit{Tone II} - \textit{Mean} - \beta)$). Their expressions are shown in Equations (1) and (2). The piecewise functions constructed from these intervals are applicable to the segmentation of different types of borehole images.

$$[\textit{Tone I}, \textit{Mean} - \alpha] = \left[\textit{Tone I}, \sum_{k=0}^{255} \frac{k \times Z_k}{M \times N} - \alpha \right] \tag{1}$$

$$[\textit{Tone II}, \textit{Mean} - \beta] = \left[\textit{Tone II}, \sum_{k=0}^{255} \frac{k \times Z_k}{M \times N} - \beta \right] \tag{2}$$

where *Tone I* and *Tone II* correspond to the grayscale values of the first tone and the second tone ($\textit{Tone I} = 26, \textit{Tone II} = 51$); *Mean* represents the average grayscale value of the image; α and β correspond to the fluctuation values in the small-scale and large-scale visual blind spots ($\alpha = 100, \beta = 90$); k is the current grayscale value; M and N are the width and height of the image; and Z_k is the frequency of occurrence of the current grayscale value. According to the gray distribution of the image, the transformation interval suitable for the current image can be obtained.

3.3.2. Extract Visual Blind Spots

The segmented functions are constructed by using the obtained dual-scale grayscale transformation intervals for grayscale transformation, and then the binary images with large and small scales are segmented by the Otsu algorithm. After noise filtering processing, the adaptive dual-scale visual blind spot can be achieved.

With the obtained dual-scale grayscale transformation intervals ($(\textit{Tone I} - \textit{Mean} - \alpha)$ and $(\textit{Tone II} - \textit{Mean} - \beta)$), the segmented functions $F1$ and $F2$ are constructed, as shown in Equations (3) and (4). Using $F1$ and $F2$ to perform grayscale transformations on the original

image, two grayscale images of different scales of visual blind spots are obtained, as shown in Figure 6b,c.

$$F1(x, y) = \begin{cases} I(x, y) & 0 \leq I(x, y) \leq \text{Tone I} \\ \frac{G_{\max} - 0}{(\text{Mean} - \alpha) - \text{Tone I}} \times I(x, y) & \text{Tone I} < I(x, y) \leq \text{Mean} - \alpha \\ I(x, y) & \text{Mean} - \alpha < I(x, y) \leq G_{\max} \end{cases} \quad (3)$$

$$F2(x, y) = \begin{cases} I(x, y) & 0 \leq I(x, y) \leq \text{Tone II} \\ \frac{G_{\max} - 0}{(\text{Mean} - \beta) - \text{Tone II}} \times I(x, y) & \text{Tone II} < I(x, y) \leq \text{Mean} - \beta \\ I(x, y) & \text{Mean} - \beta < I(x, y) \leq G_{\max} \end{cases} \quad (4)$$

where $I(x, y)$ represents the grayscale value of pixel coordinates (x, y) in image I before grayscale transformation; $F1(x, y)$ and $F2(x, y)$ represent the grayscale values of this pixel in image I after grayscale transformation. G_{\max} is the maximum value of the grayscale range of the image. The definition domains of $F1(x, y)$ and $F2(x, y)$ are determined based on the transformation intervals in Equations (1) and (2).

The Otsu [30] algorithm is commonly used to obtain the global threshold of the image, and it can automatically find a binary threshold suitable for the current image. After obtaining the grayscale images representing two different scales of visual blind spots, we used the Otsu algorithm to binarize the grayscale images, as shown in Figure 6d,e.

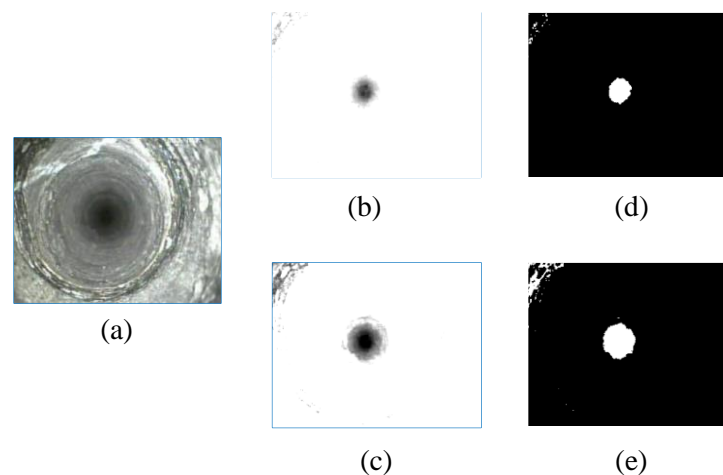


Figure 6. Flowchart of grayscale transformation and binarization process. (a) Original image. (b) Grayscale image after transformation by $F1(x, y)$. (c) Grayscale image after transformation by $F2(x, y)$. (d) Binarized image corresponding to (b). (e) Binarized image corresponding to (c).

Due to the uneven surface roughness of the hole wall and the varying attenuation of light scattering during the imaging process, the resulting binary image may have a small number of noise points and local black spots. To eliminate these interferences, this article uses the two pass connected region labeling (TPCRL) algorithm [31] to process the image to remove the noise points and local black spots.

The TPCRL algorithm is used to traverse all pixels in a binary image, attaching the same label to non-zero pixels that are connected to each other [32]. The regions composed of pixels with the same label are referred to as connected regions, and the entire image is composed of a series of connected regions with different labels. The labeling results are shown in Figure 7. The entire image is composed of 7 different connected regions, marked with different colors. The red region is the visual blind spot, which has a significantly larger area than the other regions. The remaining connected regions are the noise points and local black spots generated by regions with high attenuation of light scattering.

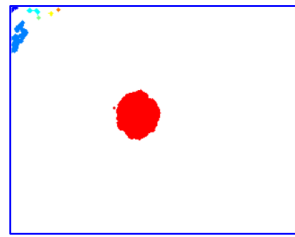


Figure 7. Connected region labeling result.

The area of each connected region (i.e., the total number of pixels in each region) was statistically analyzed, and the results are shown in Table 2. We set the threshold P and eliminate connected regions in the binary image where the number of pixels was less than P to remove noise points and small-area local black spots. Figure 8a represents the binary image before noise points and small-area local black spots were removed, Figure 8b represents the binary image after connected region detection, and Figure 8c is the result after eliminating connected regions smaller than the threshold value.

Table 2. Area statistics of connected regions.

Color	Red	Blue	Light Blue	Dark Blue	Yellow	Green	Orange
Pixels	1834	301	51	38	28	13	13

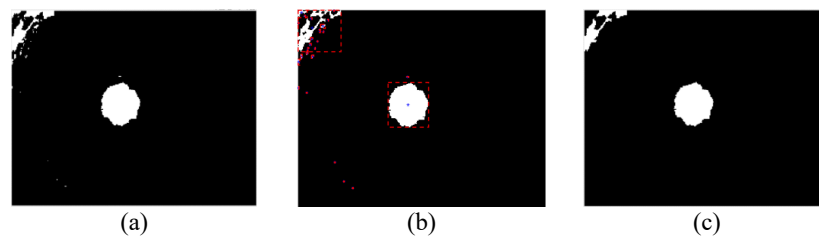


Figure 8. Image with noise points and small-area local black spots removed. (a) Binary image before removing noise points and small-area black spots. (b) Connected region detection result. (c) Noise filtering result.

Finally, by performing grayscale transformation, binarization, and connected region filtering on the original images, the dual-scale visual blind spot images are obtained. Figure 9a represents the image of the large-scale visual blind spot, and Figure 9b represents the image of the small-scale visual blind spot.

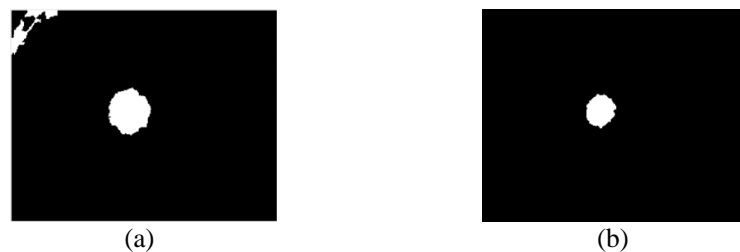


Figure 9. Dual-scale visual blind spot. (a) Large-scale visual blind spot. (b) Small-scale visual blind spot.

3.4. Segmentation of Optimal Non-Concentric Ring Regions

The optimal non-concentric ring region is segmented by the optimal outer circle and inner circle. In this section, the automatic positioning of the outer and inner circles is achieved based on both small-scale and large-scale visual blind regions.

3.4.1. Outer Circle Localization Based on Small-Scale Visual Blind Spot

Typically, the center of the optimal outer circle (i.e., the drilling center) is located at the center of the small-scale visual blind spot, as shown in Figure 10. The contour of this region is irregularly circular. In this paper, the Strong-Weighted Centroid Algorithm [33] is used to obtain the centroid coordinates of the small-scale visual blind spot as the center coordinates of the drilling hole for the positioning of the outer circle.

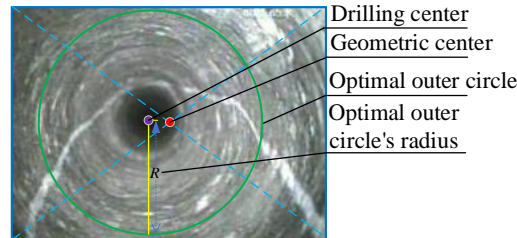


Figure 10. Schematic diagram of borehole center localization.

The Strong-Weighted Centroid Algorithm is a weighted centroid acquisition algorithm based on the given point set. This algorithm assigns weights to each point, making the contribution of each point more accurately reflected in the calculation results. Unlike traditional arithmetic averages, the Strong-Weighted Centroid Algorithm weights each point based on its geometric position; thus, it is better suited for the handling of irregular point distributions.

In the process of obtaining the center of the drilling hole, the Strong-Weighted Centroid Algorithm is used to enhance the pixel weights of some regions closer to the center of the visual blind spot, further increasing the influence of points with a greater impact on the visual blind spot, thereby improving the centroid localization accuracy. The calculation formulas are shown in Equations (5) and (6).

$$x_c = \frac{\sum_{j=y_0-w_0,y/2}^{y_0+w_0,y/2} \sum_{i=x_0-w_0,x/2}^{x_0+w_0,x/2} x_i I_{ij} w}{\sum_{j=y_0-w_0,y/2}^{y_0+w_0,y/2} \sum_{i=x_0-w_0,x/2}^{x_0+w_0,x/2} I_{ij} w} \tag{5}$$

$$y_c = \frac{\sum_{i=x_0-w_0,x/2}^{x_0+w_0,x/2} \sum_{j=y_0-w_0,y/2}^{y_0+w_0,y/2} y_j I_{ij} w}{\sum_{i=x_0-w_0,x/2}^{x_0+w_0,x/2} \sum_{j=y_0-w_0,y/2}^{y_0+w_0,y/2} I_{ij} w} \tag{6}$$

where (x_c, y_c) is the coordinate of the borehole center, (x_i, y_i) is the current pixel coordinate, I_{ij} represents the light intensity received of each pixel, and w is the weighting function, which can take various forms. In this paper, we use $w=l^a$, where a is the weighting factor, set to 3.

After obtaining the coordinates of the outer circle's center (x_c, y_c) , we need to draw a perpendicular line from this point, intersecting with the image edge to obtain the point (x_i, y_i) , and calculate the length of this perpendicular line d_i , where the shortest length of the perpendicular lines is the optimal outer circle's radius, as shown in Equation (7).

$$R = \min\{d_i\} = \min \left\{ \sqrt{(x_1 - x_0)^2 + (y_1 - y_0)^2}, \sqrt{(x_2 - x_0)^2 + (y_2 - y_0)^2}, \dots \right. \\ \left. \dots, \sqrt{(x_i - x_0)^2 + (y_i - y_0)^2} \right\} \tag{7}$$

Through the above-mentioned method, using the extracted outer circle in this article for image segmentation, it is possible to preserve the valid information of the image to the greatest extent, while eliminating the EDR. Finally, the borehole image obtained after removing the EDR is as shown in Figure 11.

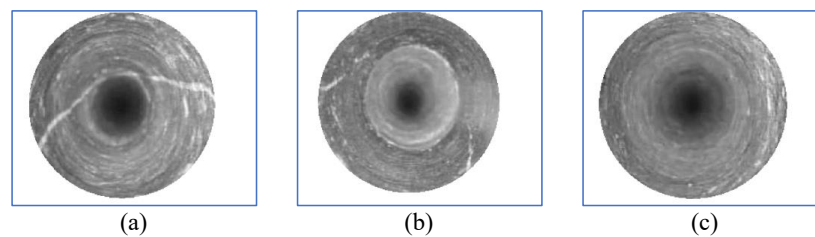


Figure 11. EDR segmentation results. (a) Fracture image. (b) Border image. (c) Intact rock image.

3.4.2. Inner Circle Localization Based on Large-Scale Visual Blind Spot

The optimal inner circle positioning method in this paper mainly includes the following three steps: edge detection, circular Hough transform, and the extraction of the optimal inner circle.

(1) Edge detection

Considering that the edge pixels in the large-scale visual blind spot often have a discontinuous distribution, this paper uses the Canny operator [34] for edge detection. It can more accurately obtain the edge information of the large-scale visual blind spots, providing a basis for the localization of the optimal inner circle.

Figure 12 shows the edge extraction results of the intact rock, fracture, and border images after applying the Canny operator. It can be observed that the edge detection results of fracture and border images contain more than two types of edge information.

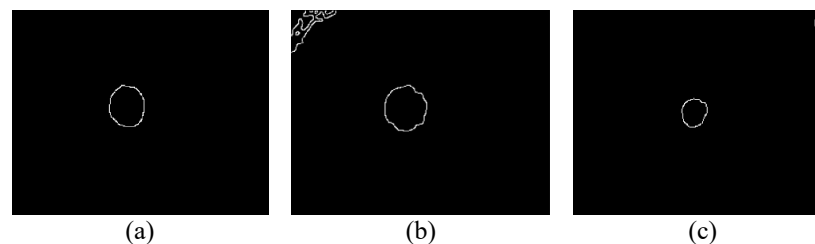


Figure 12. Canny edge detection results. (a) The edge detection results of an intact rock image. (b) The edge detection results of a fracture image. (c) The edge detection results of a border image.

(2) Circular Hough transform

The circular Hough transform [35] is an effective algorithm for the detection of circular contours in an image. It can view circular contours as a series of possible combinations of center and radius, and then search for points that match these combinations by traversing all pixels in the image. By accumulating all possible combinations of centers and radii, the Hough transform can detect the presence of circles in the image. The expression is shown in Equation (8), where the coordinates of any point on the circle can be represented by Equation (9).

$$(x - a)^2 + (y - b)^2 = r^2 \quad (8)$$

$$\begin{cases} x = a + r \cos \theta \\ y = b + r \sin \theta \end{cases} \quad (9)$$

where (x, y) can represent the coordinates of any point on the Hough circle. a and b represent the horizontal and vertical coordinates of the center of the circle, r is the radius of the circle, and θ is the angle between the normal and the x-axis.

To extract the inner circle, this article inputs the Canny edge detection results into the circular Hough transform algorithm for operation and obtains the positions and radii of all circles in the image. The results of using the circular Hough transform for three different types of images are shown in Figure 13. It can be observed that suitable Hough circles can be extracted at all locations of the visual blind spots. However, due to some local structures and image noise, there may be some interference circles in the detection result image.

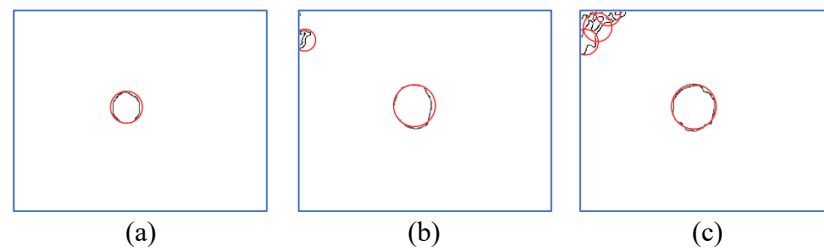


Figure 13. Circular Hough transform results. (a) Fit of the image of a single Hough circle. (b) Fit of the image of a double Hough circle. (c) Fit of an image of multiple Hough circles.

(3) Extracting the optimal inner circle

The problems with the circular Hough transform results mainly include two situations: one is the presence of multiple interfering Hough circles, and the other is that the visual blind spot is an irregular circle, and the Hough circles cannot cover all visual blind spots.

Regarding the first problem, this article first uses the Euclidean distance between the center of the Hough circle and the geometric center of the image to filter the circles. The Hough circle corresponding to the minimum Euclidean distance is selected as the target circle, eliminating other interfering circles. The calculation formula is shown in Equation (10).

$$\begin{cases} x_0 = m/2 \\ y_0 = n/2 \\ |X_i| = \sqrt{(x_i - x_0)^2 + (y_i - y_0)^2} \\ d(x_i, y_i) = \min |X_i| \end{cases} \quad (10)$$

where m and n are the width and length of the image, (x_0, y_0) is the geometric center of the image, (x_i, y_i) is the center coordinate of the i -th Hough circle, $|X_i|$ is the Euclidean distance from (x_i, y_i) to the geometric center, and $d(x_i, y_i)$ is the minimum distance of all Hough circle centers to the geometric center.

Regarding the second problem, this paper introduces a threshold γ ($\gamma = 2$) to increase the diameter of the target circle, achieving the complete coverage of the visual blind spot. As shown in Figure 14, the red circles represent the target circles obtained through the Hough transform, while the blue circles represent the optimal inner circles obtained in this study.

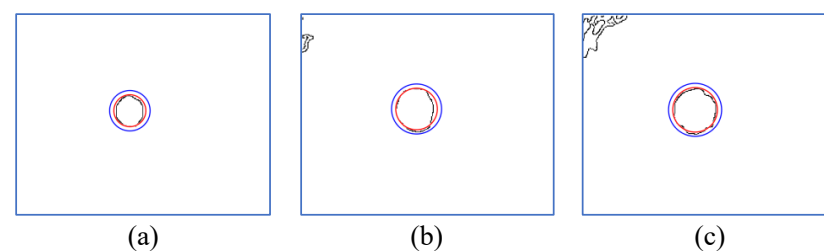


Figure 14. Optimal inner circle extraction results. (a) The processing results of the single Hough circle image. (b) The processing results of the double Hough circle image. (c) The processing results of the multiple Hough circle image.

By using the above method, utilizing the extracted optimal inner circle to perform image segmentation, it is possible to remove the QSR while preserving the maximum amount of valid image information. The final borehole image obtained after removing the QSR is shown in Figure 15.

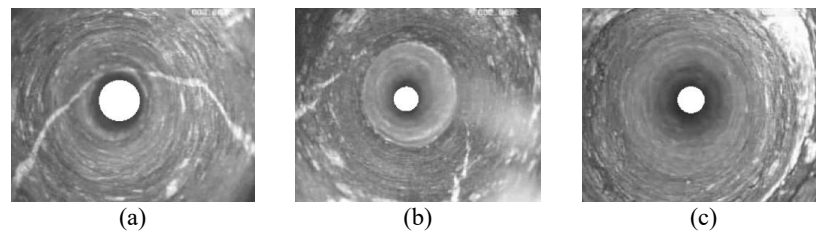


Figure 15. QSR segmentation results. (a) Fracture image. (b) Border image. (c) Intact rock image.

3.5. Dynamic Construction Method of Geological Borehole Image Recognition Database Based on ONRS Algorithm

The probe of the forward drilling camera system moves axially inside the borehole, capturing borehole images of the formation where the borehole is located, through the camera on the probe. These images are referred to as the original borehole images. Due to the influence of the environmental conditions and the illumination factors of the camera system, the original borehole images often contain extensive regions of interference, reducing the distinguishability of different types of borehole images. To enhance the performance of borehole image recognition, this paper constructs a geological borehole image recognition database based on the ONRS algorithm.

To construct the geological borehole image recognition database, first, expert knowledge is used to label the original images. Then, the ONRS algorithm is used to traverse the labeled original images to obtain the optimal non-concentric ring images. Finally, the optimal non-concentric ring images are organized and summarized to construct the geological borehole image recognition database. The method process is shown in Figure 16, and it is mainly divided into four steps.

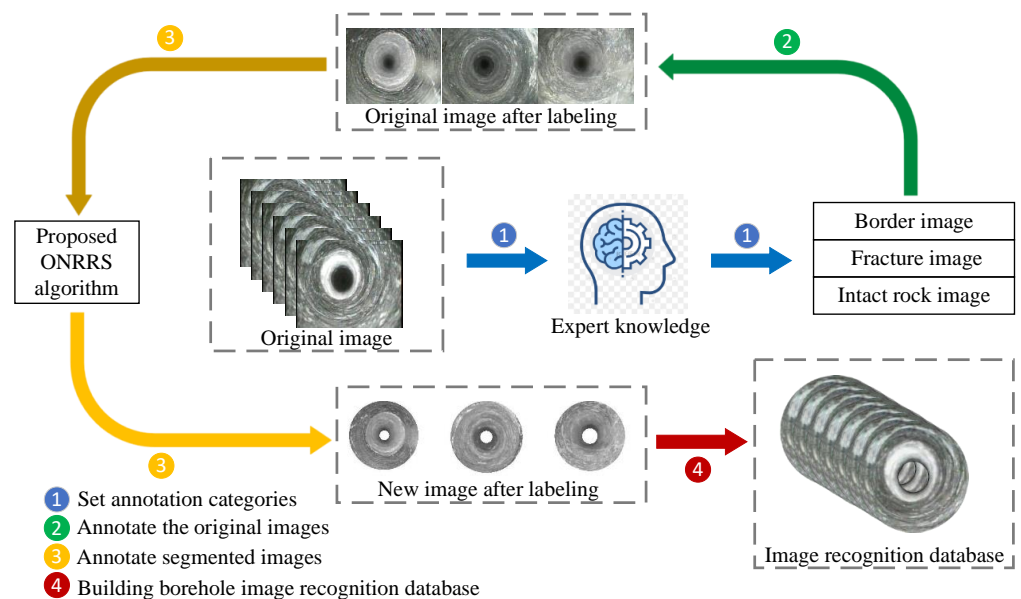


Figure 16. Dynamic construction method diagram for geological borehole image recognition database based on ONRS algorithm.

Step 1. Set the label categories. According to expert knowledge [36], the geological borehole images are generally categorized into three types, namely border images, intact rock images, and fracture images.

Step 2. Label the original images. Based on expert knowledge in the field of geology, which encompasses unique characteristic information present in various geological images, a comparative analysis of the heterogeneity among borehole images can be conducted. Subsequently, the original borehole images can be labeled according to the analysis results.

Step 3. Label the segmented images. Input the labeled original borehole images into the ONRS algorithm proposed in this paper, and the optimal non-concentric ring images with labels are obtained.

Step 4. Construct the geological borehole image recognition database. The labeled optimal non-concentric ring images are organized and categorized based on their labels, achieving the construction of the geological borehole image recognition database.

The optimal non-concentric ring images in the geological borehole image recognition database, relative to the original images, reduce the proportion of irrelevant and interfering feature information [37] while preserving effective image feature information. It is beneficial for the classification process.

4. Experimental Results and Analysis

To validate the effectiveness of the dynamic construction method of the geological borehole image recognition database, this section conducts analyses based on the image segmentation effect and image recognition performance. The dataset used in this study comprises 1410 geological borehole images, categorized into three main types, all captured in JPG format with a fixed resolution of 300×238 pixels. The experimental environment for this study includes a CPU with an Intel Core i5-11300H processor, which has a maximum main frequency of 3.10 GHz, 16 GB of RAM, and a Windows 11 operating system. The development environment employed is MATLAB R2020b.

4.1. Image Segmentation Results and Evaluation

The spatial domain processing is the primary factor affecting the image segmentation effect, and different grayscale transformation parameters will directly affect the image segmentation results in this article. This section verifies the effectiveness of the proposed ONRS algorithm utilizing different transformation parameters.

Due to the fact that the grayscale values corresponding to tonal zones IV to X of the Ansel Adams Zone System are much greater than the maximum grayscale values of the QSR, the QSR contrast cannot be improved using these grayscale values as the minimum values for the transformation interval. Furthermore, when the maximum value of the transformation interval exceeds 150, the grayscale-transformed image has no significant difference from the original image and cannot highlight the QSR. Therefore, in this section, the grayscale values corresponding to tonal zones I–III are set as the minimum values for the transformation interval. Simultaneously, values of 80, 90, *Mean*, and *Mean-β* are set as the maximum values for the transformation interval, as shown in the experimental results in Table 3.

In the vertical comparison, focusing on the experimental results where the maximum value of the transformation interval is 80, the inner circle of image (q) deviates from the center of the borehole, while the inner circles of images (r) and (j) exceed the QSR range. In the experimental results with the maximum value of 90, the inner circles of images (d), (l), (s), and (t) exceed the QSR range. In the experimental results with the maximum value of *Mean*, the inner circle in image (u) deviates from the center of the borehole, while the inner circles in other images exceed the QSR range. In contrast, the segmentation results with the maximum value of *Mean-β* outperform the others in terms of image segmentation; it does not experience the significant deviation of the inner circles from the borehole center or exceed the QSR range.

In the horizontal comparison, the segmentation results for images with different tones are compared when the maximum value is *Mean-β*. Among them, the inner circle in image (h) of *Tone I* slightly deviates from the borehole center. The inner circles in images (x) and (w) of *Tone III* exceed the QSR range. When the minimum value of the transformation interval is chosen to correspond to *Tone II*, the positioning of the inner and outer circles is relatively accurate.

Table 3. Segmentation results of non-concentric ring in different intervals.

max min	80		90		<i>Mean</i>		<i>Mean-β</i>	
<i>Tone I</i>								
	(a)	(b)	(c)	(d)	(e)	(f)	(g)	(h)
<i>Tone II</i>								
	(j)	(k)	(l)	(m)	(n)	(o)	(p)	(q)
<i>Tone III</i>								
	(q)	(r)	(s)	(t)	(u)	(v)	(w)	(x)

This indicates that the ONRS algorithm proposed in this article can obtain an ideal optimal non-concentric ring region when selecting the grayscale transformation interval corresponding to (*Tone II-Mean-β*).

In this paper, the Jaccard index and Dice similarity coefficient are used as evaluation metrics for the performance of the image segmentation algorithm. The Jaccard index [38] and Dice coefficient [39] measure the performance of the algorithm by reflecting the similarity between the actual segmentation results and the standard segmentation results. The larger the two values, the better the algorithm. They are defined as follows.

$$Jaccard = \frac{TP}{(TP + FP + FN)} \tag{11}$$

$$Dice = \frac{2 \times TP}{(2 \times TP + FP + FN)} \tag{12}$$

In this study, ten images were randomly selected from the geological borehole image recognition database. Various transformation intervals as well as the interval applied in the ONRS algorithm were evaluated. The scores of the Dice similarity coefficient and Jaccard index were recorded for comparison. Table 4 shows the experimental results in the experimental environment with an NVIDIA Titan RTX graphics card.

From Table 4, it can be observed that, compared to other transformation intervals, the Jaccard index and Dice similarity coefficient scores of the borehole images segmented using the transformation interval (*Tone II-Mean-β*) adopted in this paper are the highest. This indicates that the proposed ONRS algorithm exhibits significant advantages in borehole image segmentation.

Table 4. Scores of Dice similarity coefficient and Jaccard index for different transformation intervals.

Transformation Interval	Jaccard /%	Dice /%
(<i>Tone I</i> , 80)	87.63	98.28
(<i>Tone I</i> , 90)	87.40	98.00
(<i>Tone I</i> , <i>Mean</i>)	78.30	92.32
(<i>Tone I</i> , <i>Mean-β</i>)	88.40	98.31
(<i>Tone II</i> , 80)	87.33	98.07
(<i>Tone II</i> , 90)	87.17	97.79

Table 4. Cont.

Transformation Interval	Jaccard /%	Dice /%
(Tone II, Mean)	80.02	93.11
(Tone II, Mean- β)	88.43	98.55
(Tone III, 80)	87.33	98.07
(Tone III, 90)	86.19	97.04
(Tone III, Mean)	74.61	91.21
(Tone III, Mean- β)	87.47	98.07

4.2. Analysis of Image Recognition Performance

To validate the effectiveness of the geological borehole image recognition database constructed using the proposed method, this section verifies the recognition performance using the fine-tuned decision tree [40] (FTDT), linear SVM [41] (LSVM), fine-tuned K-nearest neighbors [42] (FT-KNN), ResNet34, and ResNet101 on both the original image database and the constructed one. In both databases, the images in the training and validation sets correspond to each other. During training, FTDT, LSVM, and FT-KNN utilize SIFT features extracted from the images as input.

First, we verify that the geological borehole image recognition database achieves higher classification accuracy. Figure 17 displays the recognition accuracy obtained with various classifiers. When classifying the two databases using FTDT, LSVM, FT-KNN, ResNet34, and ResNet101, the classification accuracy of the constructed new database is improved by 3.6%, 4.2%, 2.6%, 1.57%, and 1.05%, respectively, compared to the original image database.

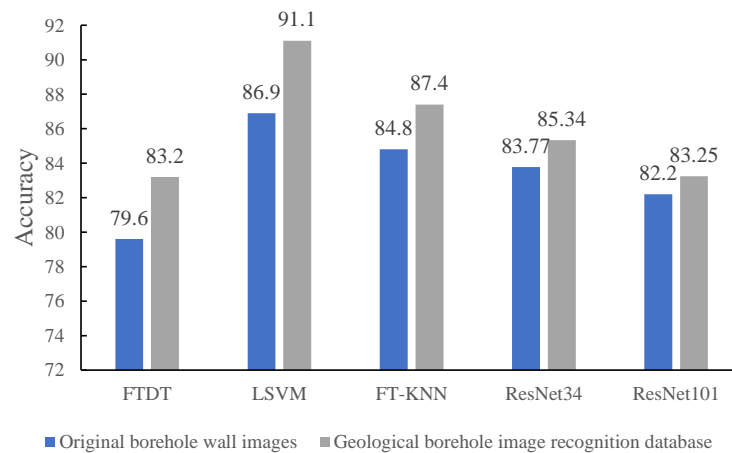


Figure 17. Classification accuracy of various algorithms on the original image database and the geological borehole image recognition database.

Next, we verify that the geological borehole image recognition database achieves higher macro-average accuracy [43]. Figure 18 presents the macro-average results for various classifiers. When classifying the two databases using FTDT, LSVM, FT-KNN, ResNet34, and ResNet101, the macro-average accuracy of the constructed new database is significantly higher than that of the original image database. The experimental data indicate that the introduction of the geological borehole image recognition database allows for the more accurate classification of images across different categories, demonstrating greater applicability.

Finally, we confirm the enhancement in class-specific accuracy achieved by the geological borehole image recognition database. To compare the results of the two databases in the aforementioned classification models, we employed a widely used indicator in statistical classification problems, namely the confusion matrix [44]. Figure 19 shows the confusion

matrix comparisons for the border images (Bi), fracture images (Fi), and intact rock images (Irm).

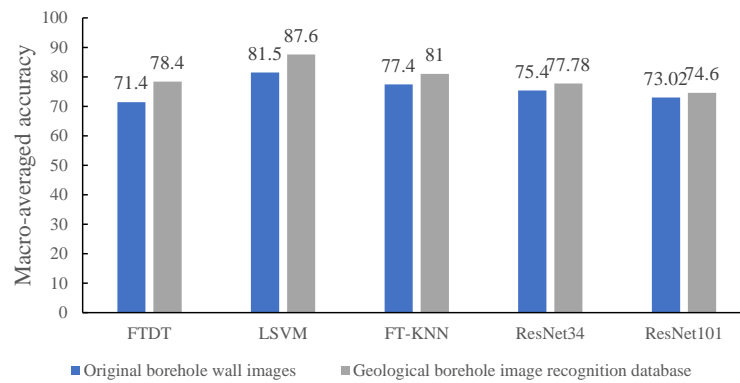


Figure 18. Macro-averaged accuracy of various classification algorithms on the original image database and the geological borehole image recognition database.

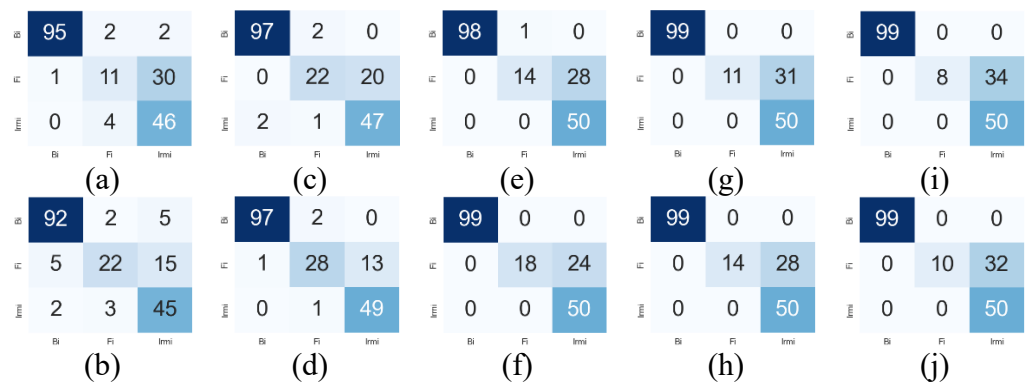


Figure 19. Confusion matrices of various classification algorithms on the original image database and the geological borehole image recognition database. (a) Classifying the original database using FTDT. (b) Classifying the new database using FTDT. (c) Classifying the original database using LSVM. (d) Classifying the new database using LSVM. (e) Classifying the original database using FT-KNN. (f) Classifying the new database using FT-KNN. (g) Classifying the original database using ResNet34. (h) Classifying the new database using ResNet34. (i) Classifying the original database using ResNet101. (j) Classifying the new database using ResNet101.

According to the confusion matrix in Figure 19, fracture images have the greatest impact on the classification accuracy of the database. Therefore, this paper mainly compares the classification results of fracture images in the original image database and the geological borehole image recognition database. Experimental analyses were conducted on both databases using FTDT, LSVM, FT-KNN, ResNet34, and ResNet101. The confusion matrix results in Figure 19a,c,e,g,i show that, in the fracture images, 30, 20, 28, 31, and 34 samples were recognized as intact rock images, respectively. The confusion matrix results in Figure 19b,d,f,h,j show that, in the fracture images, 15, 13, 24, 28, and 32 samples were recognized as intact rock images, respectively. By comparison, it can be seen that the geological borehole image recognition database proposed in this paper has higher class-specific accuracy in classifying fracture images compared to the original image database.

Based on the experimental results in this section, it is evident that under various classification models, the proposed geological borehole image recognition database has significantly improved overall accuracy compared to the original images. The improvement in the macro-average accuracy indicates that the geological borehole image recognition database achieves better average performance in cases with an uneven distribution of

categories and varying levels of category discrimination. Furthermore, the comparison of the confusion matrices validates the increase in recognition accuracy for fracture images and intact rock images when using the geological borehole image recognition database.

The conclusions from Sections 3.1 and 3.2 demonstrate that the geological borehole image recognition database shows positive applicability in processing recognition tasks on geological borehole images with special environments. The dynamic construction method for the geological borehole image recognition database demonstrates outstanding image segmentation accuracy and markedly enhances the classification precision, affirming its applicability in real-world geological drilling contexts.

5. Conclusions

Due to the influence of insufficient lighting in the shooting environment and in-hole imaging characteristics, the geological borehole images obtained contain numerous interference regions. To reduce the impact of interference regions on geological borehole image analysis and recognition work, we propose a dynamic construction method for a geological borehole image recognition database based on an optimal non-concentric ring segmentation algorithm. The optimal non-concentric ring segmentation algorithm introduces the tone of the Ansel Adams Zone System and the fluctuation value of the average grayscale value to construct the dynamic transformation interval, and it then extracts the adaptive optimal non-concentric ring region. The database construction method in this study utilizes the optimal non-concentric ring region to eliminate interference regions in the original image, ensuring the integrity of the effective regions and improving the accuracy of image recognition. The effectiveness and accuracy of this method can meet the practical needs of engineering, with potential applications in geological exploration, mineral resource investigation, and geological disaster monitoring.

Author Contributions: Conceptualization, Z.D.; methodology, S.H.; software, S.H. and Z.L.; validation, H.Z. and Z.L.; writing—original draft preparation, S.H.; writing—review and editing, Z.D.; supervision, Z.D., J.W. and H.Z. All authors have read and agreed to the published version of the manuscript.

Funding: This research was funded by Natural Science Foundation of Shandong Province (Grant No. ZR2023QF043), National Natural Science Foundation of China (Grant No. 62001263), Natural Science Foundation of Qingdao (Grant No. 23-2-1-109-zyyd-jch), Key Research Projects of Qingdao Science and Technology Plan (Grant No. 22-3-3-hygg-30-hy), National Natural Science Foundation of China under Grant (Grant No. 62173345), Major Basic Research Project of Shandong Natural Science Foundation (Grant No. ZR2022ZD38).

Data Availability Statement: Data are contained within the article.

Conflicts of Interest: The authors declare no conflicts of interest.

References

1. Deng, Z.; Song, S.; Han, S.; Liu, Z.; Wang, Q.; Jiang, L. Geological Borehole Video Image Stitching Method Based on Local Homography Matrix Offset Optimization. *Sensors* **2023**, *23*, 632. [[CrossRef](#)]
2. Xie, X.; Zhang, H.; Wang, J.; Chang, Q.; Wang, J.; Pal, N.R. Learning optimized structure of neural networks by hidden node pruning with L_1 regularization. *IEEE Trans. Cybern.* **2019**, *50*, 1333–1346. [[CrossRef](#)]
3. Wang, J.; Zhang, B.; Sang, Z.; Liu, Y.; Wu, S.; Miao, Q. Convergence of a modified gradient-based learning algorithm with penalty for single-hidden-layer feed-forward networks. *Neural Comput. Appl.* **2020**, *32*, 2445–2456. [[CrossRef](#)]
4. Gong, K.; Johnson, K.; El Fakhri, G.; Li, Q.; Pan, T. PET image denoising based on denoising diffusion probabilistic model. *Eur. J. Nucl. Med. Mol. Imaging* **2023**, *51*, 358–368. [[CrossRef](#)]
5. Hu, T.; Zhou, Q.; Nan, X.; Lin, R. A color image decomposition model for image enhancement. *Neurocomputing* **2023**, *558*, 126772. [[CrossRef](#)]
6. LaLonde, R.; Xu, Z.; Irmakci, I.; Jain, S.; Bagci, U. Capsules for biomedical image segmentation. *Med. Image Anal.* **2021**, *68*, 101889. [[CrossRef](#)]
7. SU, A.; PP, F.R.; Abraham, A.; Stephen, D. Deep Learning-Based BoVW–CRNN Model for Lung Tumor Detection in Nano-Segmented CT Images. *Electronics* **2022**, *12*, 14. [[CrossRef](#)]

8. Mohan, P.; Veerappampalayam Easwaramoorthy, S.; Subramani, N.; Subramanian, M.; Meckanzi, S. Handcrafted deep-feature-based brain tumor detection and classification using mri images. *Electronics* **2022**, *11*, 4178. [[CrossRef](#)]
9. Wang, Z.Y.; Kang, D.K.; Zhang, C.P. S2AC: Self-Supervised Attention Correlation Alignment Based on Mahalanobis Distance for Image Recognition. *Electronics* **2023**, *12*, 4419. [[CrossRef](#)]
10. Ju, Y.; Shi, B.; Chen, Y.; Zhou, H.; Dong, J.; Lam, K.M. GR-PSN: Learning to estimate surface normal and reconstruct photometric stereo images. *IEEE Trans. Vis. Comput. Graph.* **2023**, *3*, 37922172. [[CrossRef](#)]
11. Ju, Y.; Jian, M.; Wang, C.; Zhang, C.; Dong, J.; Lam, K.M. Estimating high-resolution surface normals via low-resolution photometric stereo images. *IEEE Trans. Circuits Syst. Video Technol.* **2023**. [[CrossRef](#)]
12. Zou, X.; Wang, C.; Song, H. Applications of high-resolution borehole image rapid synthesis method for the refined detection of in-suit rock mass structural features during deep-buried geotechnical engineering. *Int. J. Numer. Anal. Methods Geomech.* **2021**, *45*, 2565–2580. [[CrossRef](#)]
13. Guo, J.; Wang, Z.; Li, C.; Li, F.; Jessell, M.W.; Wu, L.; Wang, J. Multiple-point geostatistics-based three-dimensional automatic geological modeling and uncertainty analysis for borehole data. *Nat. Resour. Res.* **2022**, *31*, 2347–2367. [[CrossRef](#)]
14. Mirkes, E.M.; Gorban, A.N.; Levesley, J.; Elkington, P.A.; Whetton, J.A. Pseudo-outcrop visualization of borehole images and core scans. *Math. Geosci.* **2017**, *49*, 947–964. [[CrossRef](#)]
15. Ma, M.; Gui, Z.; Gao, Z. Research on a High-Performance Rock Image Classification Method. *Electronics* **2023**, *12*, 4805. [[CrossRef](#)]
16. Zhou, Y.; Wong, L.N.Y.; Tse, K.K.C. Novel Rock Image Classification: The Proposal and Implementation of HKUDES_Net. *Rock Mech. Rock Eng.* **2023**, *56*, 3825–3841. [[CrossRef](#)]
17. Gritzman, A.D.; Postema, M.; Rubin, D.M.; Aharonson, V. Threshold-based outer lip segmentation using support vector regression. *Signal, Image Video Process.* **2021**, *15*, 1197–1202. [[CrossRef](#)]
18. Yadav, N.K.; Saraswat, M. A novel fuzzy clustering based method for image segmentation in RGB-D images. *Eng. Appl. Artif. Intell.* **2022**, *111*. [[CrossRef](#)]
19. Matić, T.; Aleksi, I.; Hocenski, Ž.; Kraus, D. Real-time biscuit tile image segmentation method based on edge detection. *ISA Trans.* **2018**, *76*, 246–254. [[CrossRef](#)]
20. López, L.O.; Orts, F.; Ortega, G.; González-Ruiz, V.; Garzón, E.M. Fault-tolerant quantum algorithm for dual-threshold image segmentation. *J. Supercomput.* **2023**, *79*, 12549–12562. [[CrossRef](#)]
21. Bayá, A.E.; Larese, M.G.; Namías, R. Clustering stability for automated color image segmentation. *Expert Syst. Appl.* **2017**, *86*, 258–273. [[CrossRef](#)]
22. Solomon, E.; Woubie, A.; Cios, K.J. UFace: An Unsupervised Deep Learning Face Verification System. *Electronics* **2022**, *11*, 3909. [[CrossRef](#)]
23. Manjón, J.V.; Romero, J.E.; Coupe, P. A novel deep learning based hippocampus subfield segmentation method. *Sci. Rep.* **2022**, *12*, 1333. [[CrossRef](#)]
24. Zhang, B.; Liu, Y.; Cao, J.; Wu, S.; Wang, J. Fully complex conjugate gradient-based neural networks using Wirtinger calculus framework: Deterministic convergence and its application. *Neural Netw.* **2019**, *115*, 50–64. [[CrossRef](#)]
25. Islam, M.T.; Khan, H.A.; Naveed, K.; Nauman, A.; Gulfam, S.M.; Kim, S.W. LUVS-Net: A Lightweight U-Net Vessel Segmentor for Retinal Vasculature Detection in Fundus Images. *Electronics* **2023**, *12*, 1786. [[CrossRef](#)]
26. Fan, Z.; Lu, J.; Wei, C.; Huang, H.; Cai, X.; Chen, X. A hierarchical image matting model for blood vessel segmentation in fundus images. *IEEE Trans. Image Process.* **2018**, *28*, 2367–2377. [[CrossRef](#)]
27. Li, M.; He, X.; Duan, Y.; Yang, M. Experimental study on the influence of external factors on image features of coal and gangue. *Int. J. Coal Prep. Util.* **2022**, *42*, 2770–2787. [[CrossRef](#)]
28. Zhang, H.; Pu, Y.F.; Xie, X.; Zhang, B.; Wang, J.; Huang, T. A global neural network learning machine: Coupled integer and fractional calculus operator with an adaptive learning scheme. *Neural Netw.* **2021**, *143*, 386–399. [[CrossRef](#)]
29. Adams, A. *The Negative: Exposure and Development*; Bulfinch Press: Boston, MA, USA, 1995.
30. Huang, C.; Li, X.; Wen, Y. AN OTSU image segmentation based on fruitfly optimization algorithm. *Alex. Eng. J.* **2021**, *60*, 183–188. [[CrossRef](#)]
31. Doube, M. Multithreaded two-pass connected components labelling and particle analysis in ImageJ. *R. Soc. Open Sci.* **2021**, *8*, 201784. [[CrossRef](#)]
32. Bolelli, F.; Allegretti, S.; Baraldi, L.; Grana, C. Spaghetti labeling: Directed acyclic graphs for block-based connected components labeling. *IEEE Trans. Image Process.* **2019**, *29*, 1999–2012. [[CrossRef](#)]
33. Kim, K.Y.; Shin, Y. A distance boundary with virtual nodes for the weighted centroid localization algorithm. *Sensors* **2018**, *18*, 1054. [[CrossRef](#)]
34. Lu, Y.; Duanmu, L.; Zhai, Z.J.; Wang, Z. Application and improvement of Canny edge-detection algorithm for exterior wall hollowing detection using infrared thermal images. *Energy Build.* **2022**, *274*, 112421. [[CrossRef](#)]
35. Zhao, K.; Han, Q.; Zhang, C.B.; Xu, J.; Cheng, M.M. Deep hough transform for semantic line detection. *IEEE Trans. Pattern Anal. Mach. Intell.* **2021**, *44*, 4793–4806. [[CrossRef](#)]
36. Stokes, G.L.; Lynch, A.J.; Funge-Smith, S.; Valbo-Jørgensen, J.; Beard, T.D., Jr.; Lowe, B.S.; Wong, J.P.; Smidt, S.J. A global dataset of inland fisheries expert knowledge. *Sci. Data* **2021**, *8*, 182. [[CrossRef](#)]
37. Xue, G.; Wang, J.; Yuan, B.; Dai, C. DG-ALETSK: A High-Dimensional Fuzzy Approach With Simultaneous Feature Selection and Rule Extraction. *IEEE Trans. Fuzzy Syst.* **2023**, *31*, 3866–3880. [[CrossRef](#)]

38. Tang, M.; Kaymaz, Y.; Logeman, B.L.; Eichhorn, S.; Liang, Z.S.; Dulac, C.; Sackton, T.B. Evaluating single-cell cluster stability using the Jaccard similarity index. *Bioinformatics* **2021**, *37*, 2212–2214. [[CrossRef](#)]
39. Jha, S.; Kumar, R.; Priyadarshini, I.; Smarandache, F.; Long, H.V. Neutrosophic image segmentation with dice coefficients. *Measurement* **2019**, *134*, 762–772. [[CrossRef](#)]
40. Lu, H.; Ma, X. Hybrid decision tree-based machine learning models for short-term water quality prediction. *Chemosphere* **2020**, *249*, 126169. [[CrossRef](#)]
41. Nie, F.; Zhu, W.; Li, X. Decision Tree SVM: An extension of linear SVM for non-linear classification. *Neurocomputing* **2020**, *401*, 153–159. [[CrossRef](#)]
42. El Hindi, K.M.; Aljulaidan, R.R.; AlSalman, H. Lazy fine-tuning algorithms for naïve Bayesian text classification. *Appl. Soft Comput.* **2020**, *96*, 106652. [[CrossRef](#)]
43. Berger, A.; Guda, S. Threshold optimization for F measure of macro-averaged precision and recall. *Pattern Recognit.* **2020**, *102*, 107250. [[CrossRef](#)]
44. Gilbraith, W.E.; Celani, C.P.; Booksh, K.S. Visualization of confusion matrices with network graphs. *J. Chemom.* **2023**, *37*, e3435. [[CrossRef](#)]

Disclaimer/Publisher’s Note: The statements, opinions and data contained in all publications are solely those of the individual author(s) and contributor(s) and not of MDPI and/or the editor(s). MDPI and/or the editor(s) disclaim responsibility for any injury to people or property resulting from any ideas, methods, instructions or products referred to in the content.